

Multi-Linear Kernel Regression and Imputation in Data Manifolds

Duc Thien Nguyen and Konstantinos Slavakis*

Abstract—This paper introduces an efficient multi-linear non-parametric (kernel-based) approximation framework for data regression and imputation, and its application to dynamic magnetic-resonance imaging (dMRI). Data features are assumed to reside in or close to a smooth manifold embedded in a reproducing kernel Hilbert space. Landmark points are identified to describe concisely the point cloud of features by linear approximating patches which mimic the concept of tangent spaces to smooth manifolds. The multi-linear model effects dimensionality reduction, enables efficient computations, and extracts data patterns and their geometry without any training data or additional information. Numerical tests on dMRI data under severe under-sampling demonstrate remarkable improvements in efficiency and accuracy of the proposed approach over its predecessors, popular data modeling methods, as well as recent tensor-based and deep-image-prior schemes.

Index Terms—Imputation, kernel, manifold, MRI, regression.

I. INTRODUCTION

DYNAMIC magnetic resonance imaging (dMRI) is a popular non-invasive imaging modality for observing body organ movement, with rich potential in cardiac and neurological diagnosis [1]. DMRI stands out as an application domain where regression grapples with all of the archetypal data-analytic bottlenecks: large dimensionality due to the image data, dynamic data patterns due to dMRI’s time component, missing data due to under-sampling, and strong but unknown spatio-temporal correlations since, often, dMRI monitors structured movement; e.g., a beating heart [2].

It comes, thus, as no surprise that numerous data-modeling approaches have been proposed for regression and imputation on dMRI data: compressed sensing [3]–[6], low-rank models [7]–[9], and learning strategies based on dictionaries [10]–[14], transforms [15], manifolds [16]–[20], kernels [21]–[23], and tensors [24]–[27]. Recent efforts on imputation-by-regression revolve also around deep-learning (DeepL) approaches [28]–[31], which rely on time-consuming processes to learn from training data prior to reconstructing test data. Notwithstanding, concerns were raised in [32] via numerical tests which highlighted potential instabilities of DeepL approaches. Motivated by deep image priors (DIP), DeepL networks have also been used as implicit structural priors in regression for dMRI to avoid the use of training data and potential over-fitting issues [33], [34].

Departing from all of the previous schemes, this paper offers an extension of the novel nonparametric data-modeling approach of [35], [36], coined hereafter *multi-linear kernel regression and imputation in data manifolds (MultiL-KRIM)*. MultiL-KRIM introduces a multi-linear matrix decomposition

in data modeling to offer two-pronged innovation over its bi-linear predecessors KRIM [36] and BiLMDM [35]: (i) unlike KRIM and BiLMDM, where dimensionality-reduction *pre-steps* are disassociated from the regression task, MultiL-KRIM connects dimensionality reduction directly with the regression task by enabling its inverse-problem solution to identify the “optimal” dimensionality-reduced rendition of a kernel matrix which contributes in minimum data-recovery error; and (ii) it exploits its multiple matrix factors to promote efficient computations in its inverse-problem algorithmic solution.

MultiL-KRIM retains also the attributes which differentiate KRIM and BiLMDM from state-of-the-art modeling approaches: unlike low-rank [7]–[9], [15], dictionary-learning [10]–[14] and tensor [24]–[27] models, which promote a “blind decomposition” of the data matrix/tensor, MultiL-KRIM incorporates the underlying data-manifold geometry directly into data representations, but not via graph-Laplacian-matrix regularizers which are widely used in manifold-learning approaches [16]–[18]. MultiL-KRIM adopts instead a “collaborative-filtering” modeling approach to identify “optimal” and manifold-cognizant combinations of the observed data features for regression and imputation. MultiL-KRIM needs no training data to operate, builds a nonparametric regression estimate to reduce the dependence of its modeling assumptions on the probability distribution of the data [37], and offers an explainable learning paradigm via simple geometric arguments, unlike DeepL schemes, which are based, in general, on perplexed and cascading non-linear function layers.

Numerical tests on synthetic dMRI data show that MultiL-KRIM outperforms several state-of-the-art methods, including the total-variation tensor-based scheme [27] and the deep-image-prior (DIP) propelled [34], while matching at the same time the recovery-error performance of its predecessor KRIM [35], [36], but with computational times which are lower than and can reach down to one-third of those of KRIM.

II. DATA COLLECTION AND FORMATION IN dMRI

DMRI data take the form of a complex-valued (\mathbb{C} is the set of all complex numbers) three-way tensor \mathcal{Y} defined on the $(N_f \times N_p \times N_{fr})$ -sized “(k,t)-space” (Fig. 1a), with $N_f, N_p, N_{fr} \in \mathbb{N}_*$ (\mathbb{N}_* is the set of all positive integers). In the seldom case where the k-space is “fully sampled,” the “slice/frame” \mathcal{Y}_t of \mathcal{Y} (t denotes discrete time with $t \in \{1, \dots, N_{fr}\}$) collects the $(N_f \times N_p)$ -sized “k-space” measurements at t . In practice, it is often the case that the k-space data is heavily under-sampled due to physical limitations [2]. Popular sampling strategies are 1-D Cartesian (Fig. 1b) and radial (Fig. 1c) sampling. Sampling is denoted by the entry-wise *sampling mapping* $\mathcal{S}(\cdot) : \mathcal{Y}_t \mapsto \mathcal{S}(\mathcal{Y}_t)$, which nullifies

*D. T. Nguyen and K. Slavakis are with the Department of Information and Communications Engineering, Tokyo Institute of Technology, Tokyo, Japan (e-mails: {nguyen.t.au, slavakis.k.aa}@m.titech.ac.jp).

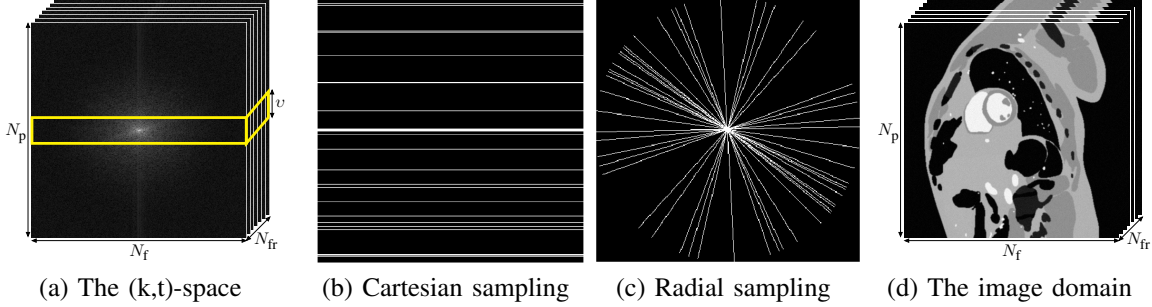


Fig. 1. (a) Complex-valued $N_f \times N_p \times N_{fr}$ (k,t)-space dMRI data. The marked $N_f \times \nu \times N_{fr}$ box corresponds to the location of the faithful data, also known as “navigator/pilot” data in dMRI. (b) 1D Cartesian and (c) radial sampling trajectories in k-space. (d) Complex-valued $N_f \times N_p \times N_{fr}$ image-domain data.

the entry of \mathcal{Y}_t when that entry is missing, while retains the entry when that entry is successfully collected. Integers N_f and N_p denote the numbers of frequency- and phase-encoding lines, respectively [1], while $N_k := N_f N_p$ represents the number of entries of each k-space frame. Typically, k-space is considered as the “frequency domain” of the “image-data” domain (Fig. 1d), so that $\mathcal{X}_t := \mathcal{F}^{-1}(\mathcal{Y}_t)$, where $\mathcal{F}^{-1}(\cdot)$ is the 2D inverse DFT [1]. For convenience, the columns of \mathcal{Y}_t are stacked one below the other to create a single $N_k \times 1$ vector $\mathbf{y}_t := \text{vec}(\mathcal{Y}_t)$ and $\mathbf{Y} := [\mathbf{y}_1, \dots, \mathbf{y}_{N_{fr}}] \in \mathbb{C}^{N_k \times N_{fr}}$.

It is often the case in an imputation framework for a subset of the sampled data to be considered *faithful*. In the present context, the “low-frequency” region, i.e., the central region of k-space, constitutes the faithful data from which geometric information will be extracted [35], [36]. These data will be called “navigator/pilot data.” The navigator data of the frame \mathcal{Y}_t (Fig. 1a) are gathered into the $\nu \times 1$ vector $\check{\mathbf{y}}_t^f$, where $\nu := \nu N_{fr}$. All of these vectors are finally stacked into the columns of $\check{\mathbf{Y}}_f := [\check{\mathbf{y}}_1^f, \dots, \check{\mathbf{y}}_{N_{fr}}^f] \in \mathbb{C}^{\nu \times N_{fr}}$.

To offer an algorithmic scheme with manageable computational complexity as the cardinality of the point-cloud $\{\check{\mathbf{y}}_t^f\}_{t=1}^{N_{fr}}$ grows for datasets with large N_{fr} , a subset $\{\mathbf{l}_k\}_{k=1}^{N_l}$, coined *landmark/representative* points, with $N_l \leq N_{fr}$, is selected from $\{\check{\mathbf{y}}_t^f\}_{t=1}^{N_{fr}}$. Any selection strategy can be used to identify $\{\mathbf{l}_k\}_{k=1}^{N_l}$. Here, the min-max-distance strategy of [38] is adopted along the lines of [35], [36]. For convenience, let the $\nu \times N_l$ matrix $\mathbf{L} := [\mathbf{l}_1, \mathbf{l}_2, \dots, \mathbf{l}_{N_l}]$.

III. DATA MODELING

With $\varphi(\cdot)$ denoting the feature mapping which maps vector \mathbf{l}_k to vector $\varphi(\mathbf{l}_k)$ in the feature space \mathcal{H} , the crux of the modeling approach is that $\{\varphi(\mathbf{l}_k)\}_{k=1}^{N_l}$ lie into or close to an unknown-to-the-user smooth manifold \mathcal{M} [39] embedded in \mathcal{H} ; see Fig. 2. To provide structured solutions, it is assumed that \mathcal{H} is a reproducing kernel Hilbert space (RKHS), equipped with a reproducing kernel $\kappa(\cdot, \cdot) : \mathbb{C}^\nu \times \mathbb{C}^\nu \rightarrow \mathbb{C}$, with well-documented merits in approximation theory [40]. To this end, the feature mapping $\varphi(\cdot)$ is defined as the mapping induced by the kernel κ of \mathcal{H} ; cf., [36]. A complex-valued \mathcal{H} is considered here [36], [41].

The (i, t) th entry y_{it} of data \mathbf{Y} is approximated as $y_{it} \approx f_i(\check{\boldsymbol{\mu}}_t)$, where $f_i(\cdot) : \mathbb{C}^\nu \rightarrow \mathbb{C}$ is an unknown non-linear function that belongs to the functional space \mathcal{H} , and $\check{\boldsymbol{\mu}}_t$ is

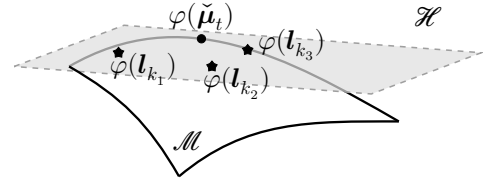


Fig. 2. A “collaborative-filtering” approach: Points $\{\varphi(\mathbf{l}_{k_j})\}_{j=1}^3$, which lie into or close to the unknown-to-the-user manifold $\mathcal{M} \subset \mathcal{H}$, collaborate affinely to approximate $\varphi(\check{\boldsymbol{\mu}}_t)$. All affine combinations of $\{\varphi(\mathbf{l}_{k_j})\}_{j=1}^3$ define the approximating “linear patch” (gray-colored plane), which mimics the concept of a tangent space to \mathcal{M} .

an unknown complex-valued $\nu \times 1$ vector. The well-known reproducing property [40] of the RKHS \mathcal{H} suggests that $y_{it} \approx f_i(\check{\boldsymbol{\mu}}_t) = \langle f_i | \varphi(\check{\boldsymbol{\mu}}_t) \rangle_{\mathcal{H}}$, where $\langle \cdot | \cdot \rangle_{\mathcal{H}}$ stands for the inner product of \mathcal{H} .

The concept of tangent spaces [39] (“linear patches” in simple words) to manifolds will be used to model both f_i and $\varphi(\check{\boldsymbol{\mu}}_t)$. Specifically, it is assumed that (i) f_i belongs to the linear span of $\{\varphi(\mathbf{l}_k)\}_{k=1}^{N_l}$, i.e., there exists $\mathbf{d}_i := [d_{i1}, \dots, d_{iN_l}]^\top \in \mathbb{C}^{N_l}$ (\top denotes vector/matrix transposition) s.t. $f_i = \sum_{k=1}^{N_l} d_{ik} \varphi(\mathbf{l}_k) = \Phi(\mathbf{L})\mathbf{d}_i$, where $\Phi(\mathbf{L}) := [\varphi(\mathbf{l}_1), \dots, \varphi(\mathbf{l}_{N_l})]$; and (ii) $\varphi(\check{\boldsymbol{\mu}}_t)$ lies into or close to \mathcal{M} and is approximated *affinely* by only a few members of $\{\varphi(\mathbf{l}_k)\}_{k=1}^{N_l}$, i.e., there exists a sparse $N_l \times 1$ vector \mathbf{b}_t s.t. $\varphi(\check{\boldsymbol{\mu}}_t) = \Phi(\mathbf{L})\mathbf{b}_t$, under the affine constraint $\mathbf{1}_{N_l}^H \mathbf{b}_t = 1$, where $\mathbf{1}_{N_l}$ is the $N_l \times 1$ all-one vector and \mathbf{H} denotes complex conjugate vector/matrix transposition; cf., Fig. 2.

In other words, $y_{it} \approx f_i(\check{\boldsymbol{\mu}}_t) = \langle f_i | \varphi(\check{\boldsymbol{\mu}}_t) \rangle_{\mathcal{H}} = \langle \Phi(\mathbf{L})\mathbf{d}_i | \Phi(\mathbf{L})\mathbf{b}_t \rangle_{\mathcal{H}} = \mathbf{d}_i^H \mathbf{K} \mathbf{b}_t$, where \mathbf{K} is the complex-valued $N_l \times N_l$ matrix whose (k, k') th entry is equal to $\langle \varphi(\mathbf{l}_k) | \varphi(\mathbf{l}_{k'}) \rangle_{\mathcal{H}} = \kappa(\mathbf{l}_k, \mathbf{l}_{k'})$. To offer compact notations, if $\mathbf{D} := [\mathbf{d}_1, \dots, \mathbf{d}_{N_k}]^H \in \mathbb{C}^{N_k \times N_l}$ and $\mathbf{B} := [\mathbf{b}_1, \dots, \mathbf{b}_{N_{fr}}] \in \mathbb{C}^{N_l \times N_{fr}}$, then data are modeled as $\mathbf{Y} \approx \mathbf{D} \mathbf{K} \mathbf{B}$.

Choosing $\kappa(\cdot, \cdot)$ to define \mathbf{K} entails the cumbersome tasks of cross validation and fine tuning via extensive experimentation on data sets. A popular way to surmount such cumbersome tasks, followed also in [36], is via multiple kernels: $\mathbf{Y} \approx \sum_{m=1}^M \mathbf{D}_m \mathbf{K}_m \mathbf{B}_m$, with a dictionary of user-defined reproducing kernels $\{\kappa_m(\cdot, \cdot)\}_{m=1}^M$, and thus kernel matrices $\{\mathbf{K}_m\}_{m=1}^M$, complex-valued $N_k \times N_l$ matrices $\{\mathbf{D}_m\}_{m=1}^M$, and $N_l \times N_{fr}$ sparse matrices $\{\mathbf{B}_m\}_{m=1}^M$ satisfying $\mathbf{1}_{N_l}^H \mathbf{B}_m = \mathbf{1}_{N_{fr}}^H$.

To reduce the computational burden and effect low-rank constraints in the resultant inverse problem, each $N_l \times N_l$ matrix \mathbf{K}_m is substituted in [36] by its low-dimensional

$d \times N_l$ rendition $\check{\mathbf{K}}_m$ in $\mathbf{Y} \approx \sum_{m=1}^M \check{\mathbf{D}}_m \check{\mathbf{K}}_m \mathbf{B}_m$, with $d \ll N_l$ and where $\{\check{\mathbf{D}}_m\}_{m=1}^M$ are low-rank $N_k \times d$ matrices. To this end, $\check{\mathbf{K}}_m$ was computed from \mathbf{K}_m via a dimensionality-reduction module (pre-step) in [36]. However, such a dimensionality-reduction pre-step introduces the following drawbacks: (i) when the numbers M of kernels and N_l of landmark points are large, the dimensionality-reduction module inflicts heavy computations, while fine-tuning its hyperparameters becomes a labor-intensive task; and (ii) the error from compressing \mathbf{K}_m into $\check{\mathbf{K}}_m$ may propagate to the next phase in the KRIM framework.

MultiL-KRIM avoids the previous drawbacks as follows:

$$\mathbf{Y} \approx \sum_{m=1}^M \mathbf{D}_m^{(1)} \mathbf{D}_m^{(2)} \dots \mathbf{D}_m^{(Q)} \mathbf{K}_m \mathbf{B}_m, \quad (1)$$

where $\mathbf{D}_m^{(q)} \in \mathbb{C}^{d_{q-1} \times d_q}$, the inner matrix dimensions $\{d_q\}_{q=1}^{Q-1}$ are user-defined, with $d_0 := N_k$ and $d_Q := N_l$. Notice that for $Q = 2$, the term $\mathbf{D}_m^{(2)} \mathbf{K}_m$ may be considered as the dimensionality-reduced $\check{\mathbf{K}}_m$ in [36]. Nonetheless, $\{\mathbf{D}_m^{(q)}\}_{(q,m)}$ are identified during a single-stage learning task, avoiding any pre-steps with their hyperparameter tuning and errors. Note that $Q > 1$ in (1) may offer considerable savings in computations with respect to the $Q = 1$ case. Indeed, the number of unknowns that need to be identified in (1) for $Q > 1$ is $N_{Q>1} = M(\sum_{q=1}^Q d_{q-1} d_q + N_{\text{fr}} N_l)$, as opposed to $N_{Q=1} = M(N_k N_l + N_{\text{fr}} N_l)$ in the $Q = 1$ case. If N_l is large, then $\{d_q\}_{q=1}^{Q-1}$ can be chosen so that $N_{Q>1} \ll N_{Q=1}$.

IV. INVERSE PROBLEM AND ITS ITERATIVE SOLUTION

Letting $\mathcal{D}_1 := [\mathbf{D}_1^{(1)}, \mathbf{D}_2^{(1)}, \dots, \mathbf{D}_M^{(1)}] \in \mathbb{C}^{N_k \times d_1 M}$, $\mathcal{B} := [\mathbf{B}_1^H, \mathbf{B}_2^H, \dots, \mathbf{B}_M^H]^H \in \mathbb{C}^{M N_l \times N_{\text{fr}}}$, and the block diagonal matrices $\mathcal{D}_q := \text{bdiag}(\mathbf{D}_1^{(q)}, \mathbf{D}_2^{(q)}, \dots, \mathbf{D}_M^{(q)}) \in \mathbb{C}^{d_{q-1} M \times d_q M}$, $q \in \{2, \dots, Q\}$, $\mathcal{K} := \text{bdiag}(\mathbf{K}_1, \mathbf{K}_2, \dots, \mathbf{K}_M) \in \mathbb{C}^{M N_l \times M N_l}$, (1) takes the form $\mathbf{Y} \approx \mathcal{D}_1 \mathcal{D}_2 \dots \mathcal{D}_Q \mathcal{K} \mathcal{B}$.

In dMRI, it is often the case that inverse problems are formulated in the image domain, since, after all, this is the domain where the end-product lies in. To this end, by using \mathbf{X} to denote the image-domain data and by defining $\mathcal{A}_1 := \mathcal{F}^{-1}(\mathcal{D}_1)$ (let also $\mathcal{A}_q := \mathcal{D}_q$, $\forall q \in \{2, \dots, Q\}$, for uniform notations), the following inverse problem is postulated:

$$\begin{aligned} \min_{\{\mathbf{X}, \mathbf{Z}, \{\mathcal{A}_q\}_{q=1}^Q, \mathcal{B}\}} & \frac{1}{2} \|\mathbf{X} - \mathcal{A}_1 \mathcal{A}_2 \dots \mathcal{A}_Q \mathcal{K} \mathcal{B}\|_{\text{F}}^2 \\ & + \lambda_1 \|\mathcal{B}\|_1 + g(\mathbf{X}, \mathbf{Z}) + h(\{\mathcal{A}_q\}_{q=1}^Q) \quad (2a) \\ \text{s.t. } & \mathcal{S}(\mathbf{Y}) = \mathcal{S} \mathcal{F}(\mathbf{X}), \quad (2b) \\ & \mathbf{1}_{N_l}^H \mathbf{B}_m = \mathbf{1}_{N_{\text{fr}}}^H, \forall m \in \{1, \dots, M\}, \quad (2c) \\ & \mathcal{A}_q \text{ is block diagonal, } \forall q \in \{2, \dots, Q\}, \quad (2d) \end{aligned}$$

where (2b) enforces consistency of the desired \mathbf{X} with the data collected in the (k,t) domain, $\|\cdot\|_1$ in (2a) is used to impose sparsity on \mathcal{B} , and the convex regularizing functions $g(\cdot)$ and $h(\cdot)$ are used to incorporate prior knowledge. More specifically, $g(\cdot)$ employs not only variable \mathbf{X} but also the auxiliary \mathbf{Z} to facilitate computations. For example, in the case where the dMRI data capture a periodic organ movement over a static background, then $g(\mathbf{X}, \mathbf{Z}) := (\lambda_2/2) \|\mathbf{Z} - \mathcal{F}_t(\mathbf{X})\|_{\text{F}}^2 +$

$\lambda_3 \|\mathbf{Z}\|_1$, where $\mathcal{F}_t(\cdot)$ stands for the temporal 1D DFT operator which acts on rows of the matrix \mathbf{X} . Note that a row of \mathbf{X} corresponds to the time series, of length N_{fr} , of a single pixel in the image domain. Additionally, the designer can choose $h(\{\mathcal{A}_q\}_{q=1}^Q) := (\lambda_4/2) \sum_{q=1}^Q \|\mathcal{A}_q\|_{\text{F}}^2$ to avoid unbounded solutions which may appear due to $\mathcal{A}_1 \mathcal{A}_2 \dots \mathcal{A}_Q$ in (2).

Algorithm 1 Solving MultiL-KRIM's inverse problem

Output: Limit point $\hat{\mathbf{X}}^{(*)}$ of sequence $(\hat{\mathbf{X}}^{(n)})_{n \in \mathbb{N}}$.

- 1: Fix $\hat{\mathcal{S}}^{(0)}$, $\gamma_0 \in (0, 1]$, and $\zeta \in (0, 1)$.
- 2: **while** $n \geq 0$ **do**
- 3: Available are $\hat{\mathcal{S}}^{(n)}$ and γ_n .
- 4: $\gamma_{n+1} := \gamma_n(1 - \zeta \gamma_n)$.
- 5: Solve sub-tasks (3).
- 6: $\hat{\mathcal{S}}^{(n+1)} := \gamma_{n+1} \hat{\mathcal{S}}^{(n+1/2)} + (1 - \gamma_{n+1}) \hat{\mathcal{S}}^{(n)}$.
- 7: Set $n \leftarrow n + 1$ and go to step 2.
- 8: **end while**

Alg. 1 sketches a solution to (2), where $\hat{\mathcal{S}}^{(n+k/2)} := (\hat{\mathbf{X}}^{(n+k/2)}, \hat{\mathbf{Z}}^{(n+k/2)}, \hat{\mathcal{A}}_1^{(n+k/2)}, \dots, \hat{\mathcal{A}}_Q^{(n+k/2)}, \hat{\mathcal{B}}^{(n+k/2)})$, $\forall n \in \mathbb{N}$, $\forall k \in \{0, 1\}$. Alg. 1 is based on the successive-convex-approximation framework of [42], which guarantees convergence to a stationary point of the loss. The following convex sub-tasks need to be solved per iteration: $\forall q \in \{1, \dots, Q\}$,

$$\begin{aligned} \hat{\mathbf{X}}^{(n+1/2)} \in \arg \min_{\mathbf{X}} & \frac{1}{2} \|\mathbf{X} - \hat{\mathcal{A}}_1^{(n)} \dots \hat{\mathcal{A}}_Q^{(n)} \mathcal{K} \hat{\mathcal{B}}^{(n)}\|_{\text{F}}^2 \\ & + \frac{\lambda_2}{2} \|\hat{\mathbf{Z}}^{(n)} - \mathcal{F}_t(\mathbf{X})\|_{\text{F}}^2 + \frac{\tau_{\text{X}}}{2} \|\mathbf{X} - \hat{\mathbf{X}}^{(n)}\|_{\text{F}}^2 \\ \text{s.t. } & \mathcal{S}(\mathbf{Y}) = \mathcal{S} \mathcal{F}(\mathbf{X}), \quad (3a) \end{aligned}$$

$$\begin{aligned} \hat{\mathbf{Z}}^{(n+1/2)} \in \arg \min_{\mathbf{Z}} & \frac{\lambda_2}{2} \|\mathbf{Z} - \mathcal{F}_t(\hat{\mathbf{X}}^{(n)})\|_{\text{F}}^2 + \lambda_3 \|\mathbf{Z}\|_1 \\ & + \frac{\tau_{\text{Z}}}{2} \|\mathbf{Z} - \hat{\mathbf{Z}}^{(n)}\|_{\text{F}}^2, \quad (3b) \end{aligned}$$

$$\begin{aligned} \hat{\mathcal{A}}_q^{(n+1/2)} \in \arg \min_{\mathcal{A}_q} & \frac{1}{2} \|\hat{\mathbf{X}}^{(n)} - \hat{\mathcal{A}}_1^{(n)} \dots \mathcal{A}_q \dots \hat{\mathcal{A}}_Q^{(n)} \mathcal{K} \hat{\mathcal{B}}^{(n)}\|_{\text{F}}^2 \\ & + \frac{\lambda_4}{2} \|\mathcal{A}_q\|_{\text{F}}^2 + \frac{\tau_{\mathcal{A}}}{2} \|\mathcal{A}_q - \hat{\mathcal{A}}_q^{(n)}\|_{\text{F}}^2 \\ \text{s.t. } & \mathcal{A}_q \text{ is block-diagonal, } \forall q \in \{2, \dots, Q\}, \quad (3c) \end{aligned}$$

$$\begin{aligned} \hat{\mathcal{B}}^{(n+1/2)} \in \arg \min_{\mathcal{B}} & \frac{1}{2} \|\hat{\mathbf{X}}^{(n)} - \hat{\mathcal{A}}_1^{(n)} \dots \hat{\mathcal{A}}_Q^{(n)} \mathcal{K} \mathcal{B}\|_{\text{F}}^2 \\ & + \lambda_1 \|\mathcal{B}\|_1 + \frac{\tau_{\mathcal{B}}}{2} \|\mathcal{B} - \hat{\mathcal{B}}^{(n)}\|_{\text{F}}^2 \\ \text{s.t. } & \mathbf{1}_{N_l}^H \mathbf{B}_m = \mathbf{1}_{N_{\text{fr}}}^H, \forall m \in \{1, \dots, M\}. \quad (3d) \end{aligned}$$

Sub-task (3d) is a composite convex minimization task under affine constraints, hence it can be solved by [43], while (3a), (3b) and (3c) have closed form solutions [36]. More specifically, the unique solution to (3b) is provided by the well-known soft-thresholding operator [36].

V. NUMERICAL TESTS

Following [9], [19], [20], [35], the proposed framework is validated on the magnetic resonance extended cardiac-torso (MRXCAT) cine phantom dataset [44] under both radial and Cartesian sampling. MultiL-KRIM[M, Q] is compared against its predecessors KRIM [36] and BiLMDM [35], as well as against the low-rank tensor factorization with total variation (LRTC-TV) [27] (designed also for dMRI data), the DIP-based

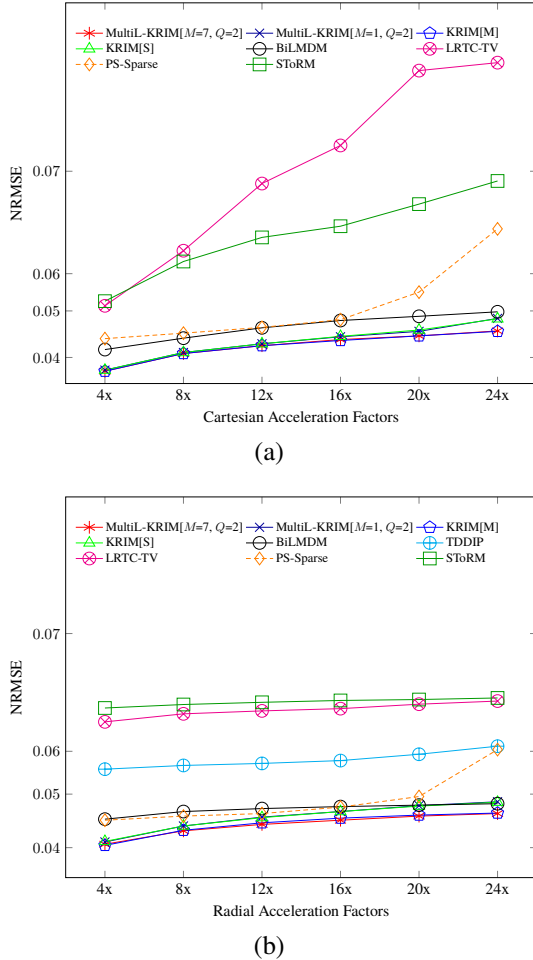


Fig. 3. NRMSE values at different Cartesian (a) and radial (b) acceleration rates. The NRMSE values are plotted on a log-axis.

TDDIP [34] (designed especially for radial sampling), and the popular PS-Sparse [9] and STORM [18]. Tags KRIM[S] and KRIM[M] refer to [36] for the case of a single ($M = 1$) and multiple ($M > 1$) kernels, respectively. Comparisons of KRIM and BiLMDM against several other state-of-the-art methods on the same data can be found in [35], [36]. All methods were finely tuned to achieve best performance.

Parameter $Q \in \{2, 3, 4\}$, and for each Q the inner matrix dimensions are set as follows: (i) if $Q = 2$, then $d_1 = 6$; (ii) if $Q = 3$, then $(d_1, d_2) = (2, 6)$; and (iii) if $Q = 4$, then $(d_1, d_2, d_3) = (2, 4, 6)$. The inner dimension parameter of KRIM is $d := 6$. Parameter $M \in \{1, 7\}$ for both MultiL-KRIM and KRIM, with choices of kernels as in [36]. Number of landmark points is $N_l := 100$. Since (2) is a non-convex task, and due to the well-known fact that the limit point of any iterative algorithm which seeks a stationary point of (2) depends on the starting point $\hat{\mathcal{S}}^{(0)}$, Alg. 1 was run multiple times for each scenario, with different $\hat{\mathcal{S}}^{(0)}$ per run, and all reported metric values are the mean values of all those multiple runs. The software code for (MultiL-)KRIM and BiLMDM was written in Julia [45]. All tests were run on an 8-core Intel(R) i7-11700 2.50GHz CPU with 32GB RAM.

The main evaluation metric is the normalized root mean square error $\text{NRMSE} := \|\mathbf{X} - \hat{\mathbf{X}}\|_F / \|\mathbf{X}\|_F$, where \mathbf{X} denotes the image data obtained from fully sampled (k,t)-space data,

and $\hat{\mathbf{X}}$ represents the estimate of \mathbf{X} . Additionally, reconstructions of high-frequency regions are evaluated by the high-frequency error norm (HFEN) and two sharpness measures M1 (intensity-variance based) and M2 (energy of the image gradient) [46], (43) and (46)]. Lastly, the structural similarity measure (SSIM) [47] captures local similarities in pixel intensities after normalizing for luminance and contrast.

It can be seen in Fig. 3, and more precisely in Tables I and II, that MultiL-KRIM matches the performance of KRIM. Nevertheless, MultiL-KRIM shows remarkable reduction in computational time by up to 65% for multiple kernels and 30% for a single kernel. To showcase that the reduction in computational time is because of the novel factorization approach, the reported times of KRIM[M] and KRIM[S] *do not* include the time of KRIM’s dimensionality-reduction pre-step. The tests also demonstrate the better performance of MultiL-KRIM over the state-of-the-art LRTC-TV and TDDIP. Notice that TDDIP takes much longer time to run on the CPU due to its deep CNN architecture. On the other hand, LRTC-TV deteriorates quickly with high acceleration rates under Cartesian sampling, with a high computational footprint.

TABLE I
PERFORMANCE ON CARTESIAN SAMPLING (ACCELERATION RATE: 20X)

Methods \ Metrics	NRMSE	SSIM	HFEN	M1	M2	Time
MultiL-KRIM[$M = 7, Q = 2$]	0.0443	0.8698	0.1147	37.26	1.4×10^6	1.2hrs
MultiL-KRIM[$M = 1, Q = 2$]	0.0453	0.8686	0.1269	37.24	1.3×10^6	46min
MultiL-KRIM[$M = 7, Q = 3$]	0.0444	0.8695	0.1149	37.26	1.4×10^6	1.3hrs
MultiL-KRIM[$M = 1, Q = 3$]	0.0454	0.8684	0.1270	37.24	1.3×10^6	42min
MultiL-KRIM[$M = 7, Q = 4$]	0.0443	0.8696	0.1147	37.26	1.4×10^6	1.4hrs
MultiL-KRIM[$M = 1, Q = 4$]	0.0453	0.8686	0.1269	37.24	1.3×10^6	43min
KRIM[M] [36]	0.0443	0.8696	0.1136	37.34	1.4×10^6	3.4hrs
KRIM[S] [36]	0.0450	0.8670	0.1149	37.25	1.3×10^6	55min
BiLMDM [35]	0.0488	0.8589	0.1423	37.08	1.3×10^6	40min
LRTC-TV [27]	0.1645	0.5942	0.3834	31.52	8.9×10^5	8.3hrs
STORM [18]	0.0850	0.8110	0.2504	37.02	1.2×10^6	58min
PS-Sparse [9]	0.0550	0.8198	0.1483	37.18	1.2×10^6	15min

TABLE II
PERFORMANCE OF RADIAL SAMPLING (ACCELERATION RATE: 16X)

Methods \ Metrics	NRMSE	SSIM	HFEN	M1	M2	Time
MultiL-KRIM[$M = 7, Q = 2$]	0.0448	0.8680	0.1023	37.35	1.4×10^6	1.1hrs
MultiL-KRIM[$M = 1, Q = 2$]	0.0465	0.8618	0.1305	37.26	1.4×10^6	44min
MultiL-KRIM[$M = 7, Q = 3$]	0.0450	0.8670	0.1130	37.35	1.4×10^6	1.2hrs
MultiL-KRIM[$M = 1, Q = 3$]	0.0465	0.8618	0.1305	37.26	1.4×10^6	41min
MultiL-KRIM[$M = 7, Q = 4$]	0.0448	0.8680	0.1023	37.35	1.4×10^6	1.2hrs
MultiL-KRIM[$M = 1, Q = 4$]	0.0465	0.8616	0.1307	37.26	1.4×10^6	42min
KRIM[M] [36]	0.0450	0.8670	0.1136	37.34	1.4×10^6	3hrs
KRIM[S] [36]	0.0465	0.8618	0.1301	37.26	1.4×10^6	58min
BiLMDM [35]	0.0475	0.8560	0.1491	37.30	1.4×10^6	1.4hrs
TDDIP [34]	0.0579	0.8167	0.2195	39.81	1.2×10^6	20hrs
LRTC-TV [27]	0.0738	0.8063	0.3725	37.06	1.7×10^6	8.6hrs
STORM [18]	0.0753	0.8319	0.3694	37.38	1.6×10^6	30min
PS-Sparse [9]	0.0496	0.7908	0.1733	37.31	1.4×10^6	15min

VI. CONCLUSIONS

This paper extends the KRIM framework [36] into a faster kernelized matrix factorization framework which avoids KRIM’s dimensionality reduction pre-step. Numerical tests demonstrate that the proposed data-modeling approach matches the reconstruction performance of KRIM under both Cartesian and radial data sampling, but with significant reduction in computational time, and outperforms at the same time popular methods as well as state-of-the-art tensor-based and deep-image-prior schemes.

REFERENCES

- [1] Z.-P. Liang and P. C. Lauterbur, *Principles of Magnetic Resonance Imaging: A Signal Processing Perspective*. IEEE Press, 2000.
- [2] Z.-P. Liang and P. C. Lauterbur, "An efficient method for dynamic magnetic resonance imaging," *IEEE Trans. Medical Imaging*, vol. 13, no. 4, pp. 677–686, 1994.
- [3] M. Lustig, D. Donoho, and J. M. Pauly, "Sparse MRI: The application of compressed sensing for rapid MR imaging," *Magnetic Resonance in Medicine*, vol. 58, no. 6, pp. 1182–1195, 2007.
- [4] U. Gamber, P. Boesiger, and S. Kozierke, "Compressed sensing in dynamic MRI," *Magnetic Resonance in Medicine*, vol. 59, no. 2, pp. 365–373, 2008.
- [5] D. Liang, E. V. R. DiBella, R.-R. Chen, and L. Ying, "k-t ISD: Dynamic cardiac MR imaging using compressed sensing with iterative support detection," *Magnetic Resonance in Medicine*, vol. 68, no. 1, pp. 41–53, 2012.
- [6] L. Feng, L. Axel, H. Chandarana, K. T. Block, D. K. Sodickson, and R. Otazo, "XD-GRASP: Golden-angle radial MRI with reconstruction of extra motion-state dimensions using compressed sensing," *Magnetic Resonance in Medicine*, vol. 75, no. 2, pp. 775–788, 2016.
- [7] R. Otazo, D. Kim, L. Axel, and D. K. Sodickson, "Combination of compressed sensing and parallel imaging for highly accelerated first-pass cardiac perfusion MRI," *Magnetic Resonance in Medicine*, vol. 64, no. 3, pp. 767–776, 2010.
- [8] S. G. Lingala, Y. Hu, E. V. R. DiBella, and M. Jacob, "Accelerated dynamic MRI exploiting sparsity and low-rank structure: k-t SLR," *IEEE Trans. Medical Imaging*, vol. 30, no. 5, pp. 1042–1054, 2011.
- [9] B. Zhao, J. P. Haldar, A. G. Christodoulou, and Z.-P. Liang, "Image reconstruction from highly undersampled (k,t)-space data with joint partial separability and sparsity constraints," *IEEE Trans. Medical Imaging*, vol. 31, no. 9, pp. 1809–1820, 2012.
- [10] S. P. Awate and E. V. R. DiBella, "Spatiotemporal dictionary learning for undersampled dynamic MRI reconstruction via joint frame-based and dictionary-based sparsity," in *Proceedings of ISBI*, pp. 318–321, 2012.
- [11] Y. Wang and L. Ying, "Compressed sensing dynamic cardiac cine MRI using learned spatiotemporal dictionary," *IEEE Trans. Biomedical Eng.*, vol. 61, no. 4, pp. 1109–1120, 2014.
- [12] J. Caballero, A. N. Price, D. Rueckert, and J. V. Hajnal, "Dictionary learning and time sparsity for dynamic MR data reconstruction," *IEEE Trans. Medical Imaging*, vol. 33, no. 4, pp. 979–994, 2014.
- [13] Y. Wang, N. Cao, Z. Liu, and Y. Zhang, "Real-time dynamic MRI using parallel dictionary learning and dynamic total variation," *Neurocomputing*, vol. 238, pp. 410–419, 2017.
- [14] S. Ravishanker, B. E. Moore, R. R. Nadakuditi, and J. A. Fessler, "Low-rank and adaptive sparse signal (LASSI) models for highly accelerated dynamic imaging," *IEEE Trans. Medical Imaging*, vol. 36, no. 5, pp. 1116–1128, 2017.
- [15] B. Wen, S. Ravishanker, and Y. Bresler, "FRIST—Flipping and rotation invariant sparsifying transform learning and applications," *Inverse Problems*, vol. 33, no. 7, p. 074007, 2017.
- [16] M. Usman, D. Atkinson, C. Kolbitsch, T. Schaeffter, and C. Prieto, "Manifold learning based ECG-free free-breathing cardiac CINE MRI," *J. Magnetic Resonance Imag.*, vol. 41, no. 6, pp. 1521–1527, 2015.
- [17] X. Chen, M. Usman, C. F. Baumgartner, D. R. Balfour, P. K. Marsden, A. J. Reader, C. Prieto, and A. P. King, "High-resolution self-gated dynamic abdominal MRI using manifold alignment," *IEEE Trans. Medical Imaging*, vol. 36, no. 4, pp. 960–971, 2017.
- [18] S. Poddar and M. Jacob, "Dynamic MRI using smoothness regularization on manifolds (SToRM)," *IEEE Trans. Medical Imaging*, vol. 35, no. 4, pp. 1106–1115, 2016.
- [19] U. Nakarmi, K. Slavakis, J. Lyu, and L. Ying, "M-MRI: A manifold-based framework to highly accelerated dynamic magnetic resonance imaging," in *Proceedings of ISBI*, pp. 19–22, 2017.
- [20] U. Nakarmi, K. Slavakis, and L. Ying, "MLS: Joint manifold-learning and sparsity-aware framework for highly accelerated dynamic magnetic resonance imaging," in *Proceedings of ISBI*, pp. 1213–1216, 2018.
- [21] U. Nakarmi, Y. Wang, J. Lyu, D. Liang, and L. Ying, "A kernel-based low-rank (KLR) model for low-dimensional manifold recovery in highly accelerated dynamic MRI," *IEEE Trans. Medical Imaging*, vol. 36, no. 11, pp. 2297–2307, 2017.
- [22] S. Poddar, Y. Q. Mohsin, D. Ansah, B. Thattaliyath, R. Ashwath, and M. Jacob, "Manifold recovery using kernel low-rank regularization: application to dynamic imaging," *IEEE Trans. Computational Imaging*, vol. 5, no. 3, pp. 478–491, 2019.
- [23] O. Arif, H. Afzal, H. Abbas, M. F. Amjad, J. Wan, and R. Nawaz, "Accelerated dynamic MRI using kernel-based low rank constraint," *J. Medical Systems*, vol. 43, no. 8, p. 271, 2019.
- [24] J. Liu, P. Musialski, P. Wonka, and J. Ye, "Tensor completion for estimating missing values in visual data," *IEEE Trans. Pattern Analysis and Machine Intelligence*, vol. 35, no. 1, pp. 208–220, 2012.
- [25] M. Signoretto, L. D. Lathauwer, and J. A. K. Suykens, "Learning tensors in reproducing kernel Hilbert spaces with multilinear spectral penalties," *arXiv:1310.4977*, 2013.
- [26] H. Kanagawa, T. Suzuki, H. Kobayashi, N. Shimizu, and Y. Tagami, "Gaussian process nonparametric tensor estimator and its minimax optimality," in *Proceedings of ICML*, vol. 48, pp. 1632–1641, 2016.
- [27] X. Li, Y. Ye, and X. Xu, "Low-rank tensor completion with total variation for visual data inpainting," *Proceedings of AAAI Conference on Artificial Intelligence*, vol. 31, Feb. 2017.
- [28] J. Schlemper, J. Caballero, J. V. Hajnal, A. N. Price, and D. Rueckert, "A deep cascade of convolutional neural networks for dynamic MR image reconstruction," *IEEE Trans. Medical Imaging*, vol. 37, no. 2, pp. 491–503, 2018.
- [29] S. Biswas, H. K. Aggarwal, and M. Jacob, "Dynamic MRI using model-based deep learning and SToRM priors: MoDL-SToRM," *Magnetic Resonance in Medicine*, vol. 82, pp. 485–494, July 2019.
- [30] D. Liang, J. Cheng, Z. Ke, and L. Ying, "Deep magnetic resonance image reconstruction: Inverse problems meet neural networks," *IEEE Signal Processing Magaz.*, vol. 37, no. 1, pp. 141–151, 2020.
- [31] C. M. Sandino, J. Y. Cheng, F. Chen, M. Mardani, J. M. Pauly, and S. S. Vasanawala, "Compressed sensing: From research to clinical practice with deep neural networks: Shortening scan times for magnetic resonance imaging," *IEEE Signal Processing Magaz.*, vol. 37, no. 1, pp. 117–127, 2020.
- [32] V. Antun, F. Renna, C. Poon, B. Adcock, and A. C. Hansen, "On instabilities of deep learning in image reconstruction and the potential costs of AI," *Proceedings of the National Academy of Sciences*, vol. 117, no. 48, pp. 30088–30095, 2020.
- [33] Q. Zou, A. H. Ahmed, P. Nagpal, S. Kruger, and M. Jacob, "Dynamic imaging using a deep generative SToRM (Gen-SToRM) model," *IEEE Trans. Medical Imaging*, vol. 40, no. 11, pp. 3102–3112, 2021.
- [34] J. Yoo, K. H. Jin, H. Gupta, J. Yerly, M. Stuber, and M. Unser, "Time-dependent deep image prior for dynamic MRI," *IEEE Trans. Medical Imaging*, vol. 40, no. 12, pp. 3337–3348, 2021.
- [35] G. N. Shetty, K. Slavakis, A. Bose, U. Nakarmi, G. Scutari, and L. Ying, "Bi-linear modeling of data manifolds for dynamic-MRI recovery," *IEEE Trans. Medical Imaging*, vol. 39, no. 3, pp. 688–702, 2020.
- [36] K. Slavakis, G. N. Shetty, L. Cannelli, G. Scutari, U. Nakarmi, and L. Ying, "Kernel regression imputation in manifolds via bi-linear modeling: The dynamic-MRI case," *IEEE Trans. Computational Imaging*, vol. 8, pp. 133–147, 2022.
- [37] L. Györfi, M. Kohler, A. Krzyżak, and H. Walk, *A Distribution-Free Theory of Nonparametric Regression*. New York: Springer, 2010.
- [38] V. De Silva and J. B. Tenenbaum, "Sparse multidimensional scaling using landmark points," tech. rep., Stanford University, 2004.
- [39] J. W. Robbin and D. A. Salamon, *Introduction to Differential Geometry*. Berlin: Springer, 2022.
- [40] N. Aronszajn, "Theory of reproducing kernels," *Trans. American Mathematical Society*, vol. 68, no. 3, pp. 337–404, 1950.
- [41] P. Bouboulis and S. Theodoridis, "Extension of Wirtinger's calculus to reproducing kernel Hilbert spaces and the complex kernel LMS," *IEEE Trans. Signal Processing*, vol. 59, no. 3, pp. 964–978, 2010.
- [42] F. Facchinei, G. Scutari, and S. Sagratella, "Parallel selective algorithms for nonconvex big data optimization," *IEEE Trans. Signal Processing*, vol. 63, no. 7, pp. 1874–1889, 2015.
- [43] K. Slavakis and I. Yamada, "Fejér-monotone hybrid steepest descent method for finely constrained and composite convex minimization tasks," *Optimization*, vol. 67, no. 11, pp. 1963–2001, 2018.
- [44] L. Wissmann, C. Santelli, W. P. Segars, and S. Kozierke, "MRXCAT: Realistic numerical phantoms for cardiovascular magnetic resonance," *J. Cardiovascular Magnetic Resonance*, vol. 16, no. 1, pp. 1–11, 2014.
- [45] J. Bezanson, A. Edelman, S. Karpinski, and V. B. Shah, "Julia: A fresh approach to numerical computing," *SIAM Review*, vol. 59, no. 1, pp. 65–98, 2017.
- [46] M. Subbarao, T.-S. Choi, and A. Nikzad, "Focusing techniques," *Optical Engineering*, vol. 32, no. 11, pp. 2824–2836, 1993.
- [47] Z. Wang, A. C. Bovik, H. R. Sheikh, and E. P. Simoncelli, "Image quality assessment: From error visibility to structural similarity," *IEEE Trans. Medical Imaging*, vol. 13, no. 4, pp. 600–612, 2004.